Decay of excited nuclei produced in ^{78,82}Kr+^{40}Ca reactions at 5.5 MeV/nucleon

G. Ademard,[1] J. P. Wieleczko,[1,*] J. Gomez del Campo,[2] M. La Commara,[3,4] E. Bonnet,[1] M. Vigilante,[3,4] A. Chbihi,[1] J. D. Frankland,[1] E. Rosato,[3,4] G. Spadaccini,[3,4] Sh. A. Kalandarov,[5,6] C. Beck,[7] S. Barlini,[8] B. Borderie,[9] R. Bougault,[10] R. Dayras,[11] G. De Angelis,[12] J. De Sanctis,[13] V. L. Kravchuk,[12] P. Lautesse,[14] N. Le Neindre,[10] J. Moisan,[1,15] A. D'Onofrio,[16] M. Parlog,[10] D. Pierroutsakou,[4] M. F. Rivet,[9] M. Romoli,[4] R. Roy,[15] G. G. Adamian,[5,6] and N. V. Antonenko[5]

[1]*Grand Accélérateur National d'Ions Lourds (GANIL), CEA/DSM-CNRS/IN2P3, Boulevard H. Becquerel, F-14076, Caen, France*
[2]*Physics Division, Oak Ridge National Laboratory, Oak Ridge, Tennessee 37831, USA*
[3]*Dipartimento di Scienze Fisiche, Università di Napoli "Federico II," I-80126, Napoli, Italy*
[4]*INFN, Sezione di Napoli, I-80126, Napoli, Italy*
[5]*Joint Institute for Nuclear Research, 141980 Dubna, Russia*
[6]*Institute of Nuclear Physics, 702132 Tashkent, Uzbekistan*
[7]*IPHC, IN2P3-CNRS, F-67037, Strasbourg Cedex 2, France*
[8]*INFN, Sezione di Firenze, I-50125 Firenze, Italy*
[9]*IPNO, IN2P3-CNRS and Université Paris-Sud 11, F-91406, Orsay Cedex, France*
[10]*LPC, IN2P3-CNRS, ENSICAEN and Université, F-14050, Caen Cedex, France*
[11]*CEA, IRFU, SPhN, CEA/Saclay, F-91191, Gif-sur-Yvette Cedex, France*
[12]*INFN, LNL, I-35020 Legnaro (Padova) Italy*
[13]*INFN, Sezione di Bologna, I-40127 Bologna, Italy*
[14]*IPNL, IN2P3-CNRS et Université, F-69622, Villeurbanne Cedex, France*
[15]*Laboratoire de Physique Nucléaire, Université de Laval, Québec, Canada G1K 7P4*
[16]*Dipartimento di Scienze Ambientali, Seconda Università di Napoli, I-81100, Caserta, Italy*

(Received 14 February 2011; published 31 May 2011)

Decay modes of excited nuclei are investigated in ^{78,82}Kr+^{40}Ca reactions at 5.5 MeV/nucleon. Charged products were measured by means of the 4π INDRA array. Kinetic-energy spectra and angular distributions of fragments with atomic number $3 \leqslant Z \leqslant 28$ indicate a high degree of relaxation and are compatible with a fissionlike phenomenon. Persistence of structure effects is evidenced from elemental cross sections (σ_Z) as well as a strong odd-even staggering (o-e-s) of the light-fragment yields. The magnitude of the staggering does not significantly depend on the neutron content of the emitting system. Fragment-particle coincidences suggest that the light partners in very asymmetric fission are emitted either cold or at excitation energies below the particle emission thresholds. The evaporation residue cross section of the ^{78}Kr+^{40}Ca reaction is slightly higher than the one measured in the ^{82}Kr+^{40}Ca reaction. The fissionlike component is larger by ~25% for the reaction having the lowest neutron-to-proton ratio. These experimental features are confronted to the predictions of theoretical models. The Hauser-Feshbach approach including the emission of fragments up to $Z = 14$ in their ground states as well as excited states does not account for the main features of σ_Z. For both reactions, the transition-state formalism reasonably reproduces the Z distribution of the fragments with charge $12 \leqslant Z \leqslant 28$. However, this model strongly overestimates the light-fragment cross sections and does not explain the o-e-s of the yields for $6 \leqslant Z \leqslant 10$. The shape of the whole Z distribution and the o-e-s of the light-fragment yields are satisfactorily reproduced within the dinuclear system framework which treats the competition among evaporation, fusion-fission, and quasifission processes. The model suggests that heavy fragments come mainly from quasifission while light fragments are predominantly populated by fusion. An underestimation of the cross sections for $16 \leqslant Z \leqslant 22$ could signal a mechanism in addition to the capture process.

DOI: 10.1103/PhysRevC.83.054619 PACS number(s): 25.70.Gh, 24.10.Pa, 24.60.Dr

I. INTRODUCTION

Heavy-ion-induced reactions are appropriate to explore the response of nuclei under stress of different nature and to delineate the degrees of freedom at work in the various bombarding energy domains. The regime of warm medium-mass ($A \sim$ 100–130) compound nuclei (CN) formed in fusion reactions at incident energies below 10 MeV/nucleon is characterized by the predominant role of the angular momentum of the emitting nuclei and of the mass (charge) asymmetry degree of freedom. An abundant literature has reported that the CN decay modes populate the whole mass (charge) range from evaporated light particles (like n, p, α) up to the symmetric fission, and the intermediate-mass fragments (IMF) in between the two extremes [1–5]. From the accumulated data one could identify two basic features of the final products: the charge distribution evolves from a U shape at low angular momentum (with a minimum at symmetry) toward a bell shape at high angular momentum (with a maximum around symmetric fission) [2]; a staggering of the fragment cross sections σ_Z is superimposed on this global feature, with a

*wieleczko@ganil.fr

 ©2011 American Physical Society

magnitude which depends on the size of the emitting nuclei and which increases as the neutron-to-proton N/Z ratio of the emitter decreases [3,6]. It has been suggested that the staggering effects reflect some properties of nuclei involved at the end of the disintegration cascade [7]. Indeed, a plausible explanation of the staggering of σ_Z would be that structure effects persist in the production mechanism and that fragments are emitted relatively cold, otherwise the subsequent decay would have blurred the fluctuations of the yields. Moreover, the neutron content of the emitter manifests itself in the magnitude of the IMF cross sections as shown in Refs. [3,6,8]. This raises the question of the N/Z dependence of the decay channels which is a relatively unknown and very attractive topic in the context of radioactive beam facilities.

On the theoretical side, sophisticated approaches have been developed to explain the complex facets of the disintegration modes. Many features of the light-particle emission are satisfactorily understood within the Hauser-Feshbach formalism [9], emphasizing the role of the available phase space at each step of the whole cascade [10]. On the other hand, the mechanism at the origin of the fragment emission from CN has stimulated numerous approaches as, for example, the multistep Hauser-Feshbach model, including emission channels up to Ca [11]; the transition-state model describing IMF emission as asymmetric fission [4,12]; the dynamical cluster-decay model assuming preformed cluster [13,14]; and the dinuclear system model aiming to treat the competition between the evaporation channel and the binary-decay channels associated to fusion and quasifission processes [15]. Those approaches are based on distinct hypotheses as well as fundamental nuclear ingredients such as the level density or the fission barriers to describe the thermal and collective properties that rule the competition between CN decay modes. It is worth noting that the N/Z degree of freedom is expected to play a crucial role on these quantities. For example, the level-density parameter is related to the effective mass, a property of the effective nucleon-nucleon interaction that is sensitive to the neutron-proton composition of the nuclei; the fission barriers depend strongly on the symmetry energy that is weakly constrained by experimental data [16]. Therefore, new experimental data on decay channels of nuclei at high angular momenta and a different N/Z ratio are sorely needed.

In addition to the decay stage, the phase of CN formation has its own crucial interest. Indeed, for more than 3 decades, a rich wealth of data have revealed the complexity of the fusion process and of the collisional stage preceding the CN formation. For example, extensive experimental and theoretical investigations have shown that the fusion mechanism at the vicinity of the barrier [17] is drastically influenced by the internal structure and N/Z ratio of the participating nuclei. Moreover, a large body of data for a wide variety of systems has demonstrated the role of dynamical effects on the fusion process and the strong inhibition of the CN formation by quasifission (QF). This phenomenon corresponds to the separation of the partners after a significant rearrangement of the mass and charge degree of freedom [18–23]. Interestingly, in medium-mass systems, it has been recently shown [15] that the competition between fusion-fission and quasifission mechanisms strongly depends on the angular momentum. This calls for new data to extend our knowledge on the influence of the dynamics on fusion process in this mass region.

Finally, we would like to stress that an accurate prediction of the IMF cross sections has important consequences. Indeed, one could perform spectroscopic studies of the residual nuclei left in excited states after the fragment emission. This kind of experiment has shown the strong selectivity of the ^{12}C emission with respect to the 3α channel [24]. An evident area for such studies is around the doubly magic ^{100}Sn since these nuclei are extremely difficult to reach by means of the standard fusion-evaporation method. However, a recent attempt [25] has suggested that the ^{12}C emission from a ^{116}Ba CN formed in the ^{58}Ni+^{58}Ni fusion reaction at $\sim$7 MeV/nucleon does not offer a valuable alternative for producing a given isotope compared to the fusion-evaporation method. Therefore a better understanding of the IMF emission from medium-mass CN at low excitation energy is required.

For these reasons we investigated the decay modes of excited nuclei produced in ^{78,82}Kr+^{40}Ca reactions at 5.5 MeV/nucleon incident energy. This energy regime is well adapted to form nuclei in a controlled way in terms of excitation energy since the incomplete-fusion process or pre-equilibrium emission are expected to be negligible. Exclusive measurements on an event-by-event basis are required to provide a characterization of the mechanism. Therefore a 4π detection apparatus with low energy thresholds and charge identification of the products is needed. The combination of both INDRA array [26] and the technique of the reverse kinematics permit us to collect high-quality data on evaporation residues and elemental cross sections of fragments. Our data set, obtained with a projectile pair differing by four neutrons, gives new insights on the influence of the neutron content on decay mechanisms that allows us to evaluate the respective merits of very popular theoretical approaches. Some preliminary results have been recently presented [27]. Here we concentrate on main features of the heavy products, and the study of the light-particle emission will be presented in a forthcoming paper.

Table I groups some quantities characterizing the ^{78,82}Kr+^{40}Ca reactions at 5.5 MeV/nucleon incident energy. CN excitation energies $E^\star$ have been calculated using mass tables [28]. $l_{\rm graz}\hbar$ is the grazing angular momentum given by a semiclassical formula. $l_{\rm pocket}\hbar$ is the angular momentum at which the pocket in the interaction potential vanishes. The potential is calculated as in Ref. [29]. $J_{\rm cr}\hbar$ is the maximum angular momentum for capture process as deduced from the dinuclear system (DNS) calculations (see Sec. V for details).

TABLE I. Quantities characterizing the studied reactions.

	^{78}Kr+^{40}Ca	^{82}Kr+^{40}Ca
$E^\star$ (MeV)	99	107
$E_{\rm c.m.}/V_B$	1.59	1.64
V_B (MeV)	91.2	90.3
N/Z	1.11	1.18
$l_{\rm graz}$	96	100
$l_{\rm pocket}$	70	73
$J_{\rm cr}$	73	75

N/Z is the neutron-to-proton ratio of the reaction and V_B is the fusion barrier [29]. Others interaction potential choices, like those compared in Ref. [30], give similar $l_{\rm pocket}$ and V_B values. As reported in Table I, the total available kinetic energy in the center-of-mass (c.m.) $E_{\rm c.m.}$ is well above the fusion barrier and the grazing angular momentum is large with respect to $l_{\rm pocket}\hbar$. Thus, in the reactions under study, we expect that the fusion process will be mainly governed by the inner pocket of the potential and, to a lesser extent, by the external fusion barrier.

The organization of the paper is as follows: the experimental procedures are described in Sec. II. Experimental results are shown in Sec. III for the inclusive data and in Sec. IV for the fragment-light particle coincidences. Section V deals with comparisons to statistical and dynamical calculations. The conclusions of this work are given in Sec. VI.

II. EXPERIMENTAL PROCEDURES

The experiment was performed at the GANIL facility in Caen. Beams of ^{78,82}Kr projectiles with energies of 5.5 MeV/nucleon impinged on self-supporting 1-mg/cm^2-thick ^{40}Ca targets. The targets were prepared from high purity foils by rolling. The contaminants, mostly oxygen and tantalum, were negligible as thoroughly checked during the data analysis.

The kinetic energy and atomic number of the ejectiles were measured by means of the 4π INDRA array. The reverse kinematics confers to the reaction products a focusing at forward angles and a momentum boost in the laboratory frame. For the experimental data reported here, a significant part of the reaction products is emitted from 3° to 45°. In this range, the INDRA array is made of eight rings comprising detection modules with three layers: an ionization chamber (IC) operated with 50 mbar (30 mbar) of C_3F_8 gas for $3^\circ \leqslant \theta_{\rm lab} \leqslant 27^\circ$ ($27^\circ \leqslant \theta_{\rm lab} \leqslant 45^\circ$), respectively; a 300-$\mu$m-thick silicon detector (Si); and a 14- or 10-cm length CsI(Tl) scintillator. The medium and backward angles from 45° to 176° are covered by eight rings equipped with IC/CsI(Tl) detectors, the ICs being operated with 30 mbar of C_3F_8 gas. For the calibration of the CsI at backward angles, one module per ring is equipped with a Si (80 μm)/SiLi (2000 μm) telescope inserted between IC and CsI. The energy calibration of the various layers was obtained by means of α particles emitted from a Cf source and from the elastic scattering of projectiles having various energies (^{75,78,82}Kr^{12+}, ^{75}As^{12+}, ^{50}Cr^{12+}, ^{100}Mo^{12+}) selected thanks to the CIME cyclotron. Energy calibration of the detectors ensured on accuracy of within 5%.

The intensity of the beams was adjusted in order to maintain a low probability for pile-up of the events and the data acquisition dead time below 25%. The reaction products were measured event by event by using two recording modes, a minimum-bias trigger based on the number M of fired telescopes. The first mode ($M \geqslant 1$) ensures the measurement of the elastic scattering for normalization purposes while the second mode ($M \geqslant 2$) permits accumulation of high statistics for the reactions of interest.

The kinetic energy and the atomic number of the detected products were deduced from the energy deposited in the IC and Si detectors, corrected for the energy losses in the target as well as in the dead zones of the various detection layers [31]. A typical example of a two-dimensional calculated spectrum used for the Z identification is shown in Fig. 1 where the horizontal (vertical) axis represents the energy deposited in the Si (IC) detector, respectively. These data were obtained at $10^\circ \leqslant \theta_{\rm lab} \leqslant 14^\circ$. Although only the fragments emitted in the forward hemisphere in the center of mass are collected, one recognizes the typical pattern of reaction products in reverse kinematics. The ridges associated to different atomic numbers are seen from $Z = 6$ up to $Z = 37$. The products with charge $3 \leqslant Z \leqslant 5$ punched through the silicon detectors and they are identified by means of a two-dimensional plot (not shown here) built with the energies collected in the Si and CsI detectors. Interesting features could be extracted from these raw data. An odd-even staggering is visible from the counting rates of the fragments up to $Z = 16$ with a stronger magnitude for fragments with charge $Z \leqslant 10$. Moreover, we clearly see a quasielastic component around $Z = 36$ which manifests with a higher statistics.

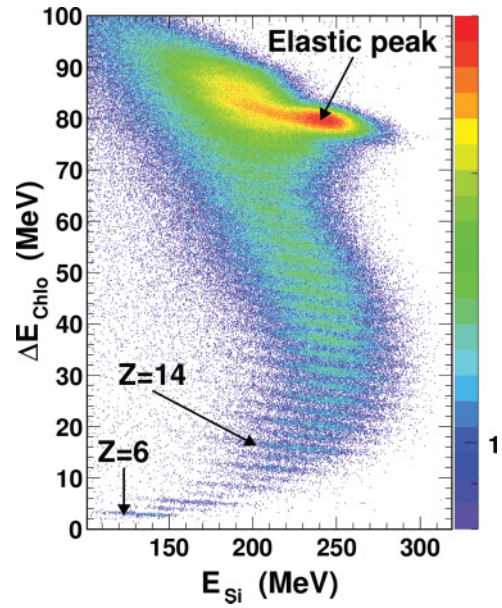

FIG. 1. (Color online) Two-dimensional plot combining the energy deposited in the ionization chamber (vertical axis) and in the silicon detector (horizontal axis) for fragments emitted at $10^\circ \leqslant \theta_{\rm lab} \leqslant 14^\circ$ measured in the ^{78}Kr+^{40}Ca reaction at 5.5 MeV/nucleon.

Event-by-event Z identification of each detected product was achieved by projecting data such as that of Fig. 1 onto lines that were drawn to follow the ridge for each Z. Charge resolution of one unit was obtained up to $Z = 37$ for high-energy fragments. Identification for low-energy fragments was assured by calculations based on energy-loss tables, with a resolution of few charge units [32]. Then we build two calculated spectra representing the total kinetic energy in the laboratory frame $E_{\rm tot}$ (the total charge $Z_{\rm tot}$) obtained by summing up the kinetic energy (the atomic number) of each particle identified in the event, respectively. In the following steps of the analysis, we kept only the events satisfying $Z_{\rm tot} \leqslant 60$ and $E_{\rm tot} \leqslant E_{\rm lab}$, where $E_{\rm lab}$ is the bombarding energy.

The limit on Z_{tot} slightly exceeds the total available charge ($Z_{tot} = 60$) to take into account the uncertainty on the charge identification. Applying such criteria enables us to control the event pile-up and double counting of the elastic scattering has been evaluated to be less than 4×10^{-6}. Consequently, the number of events comprising particles coming from two distinct reactions is negligible.

III. EXPERIMENTAL RESULTS

A. Kinematical features

Another piece of information on the reaction mechanism can be obtained from the kinetic-energy spectra of the ejectiles. The transformation into the center-of-mass frame was obtained by means of an event-by-event analysis. Figure 2 shows some representative examples of the center-of-mass kinetic-energy spectra of fragments with the indicated atomic number from $Z = 6$ to $Z = 24$ scattered at $7^\circ \leqslant \theta_{lab} \leqslant 14^\circ$ in the ^{78}Kr+^{40}Ca reaction at 5.5 MeV/nucleon. A Gaussian-like distribution (lines in Fig. 2) reproduces rather well the experimental data over a large energy range. Such a feature could be related to secondary emission of light particles and/or to shape fluctuations with the associated variations of the Coulomb barrier.

For each fragment, the center-of-mass average velocity $\langle V_{c.m.} \rangle$ was deduced from the average kinetic energy assuming a mass number given by an empirical formula [33]. The results are reported in Fig. 3 for various laboratory angles corresponding to the average values of the detection rings. For a given Z, $\langle V_{c.m.} \rangle$ is roughly the same regardless of the emission angle except for $Z \leqslant 12$ at the most forward angles. We thus conclude that a high degree of relaxation of the relative kinetic energy has been reached prior to the breakup of the excited nuclear system. $\langle V_{c.m.} \rangle$ follows a quasilinear decreases with increasing atomic charge Z. This feature is well documented ([3,4,12]) and is interpreted as a signature of a binary process dominated by the Coulomb interaction between the considered fragment and its complementary partner. The total average kinetic energy for symmetric division ($\langle \mathrm{TKE_{sym}} \rangle = 81 \pm 2$ MeV for $Z = 28$) is consistent ($E_K = 83.4$ MeV for the ^{118}Ba nucleus) with a recent compilation on the total kinetic energy release in the fission phenomenon [34].

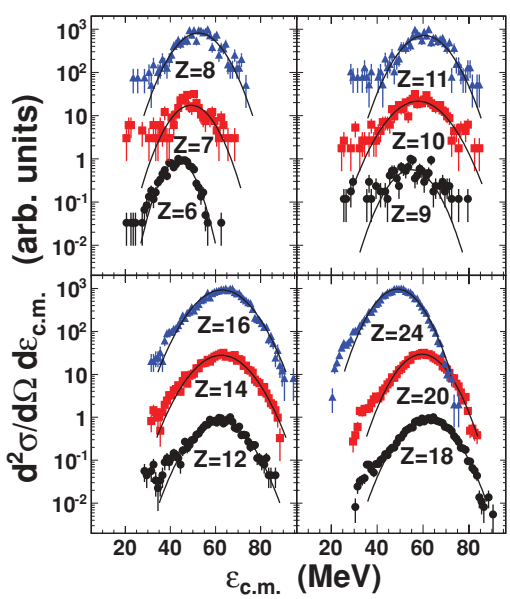

FIG. 2. (Color online) Center-of-mass kinetic-energy spectra of fragments with indicated atomic number from $Z = 6$ to $Z = 24$ produced in the ^{78}Kr+^{40}Ca reaction at 5.5 MeV/nucleon and detected at $7^\circ \leqslant \theta_{lab} \leqslant 14^\circ$. Lines represent the results of a fit with a Gaussian function. Statistical errors are shown.

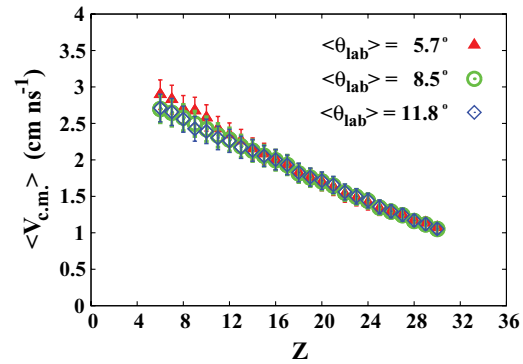

FIG. 3. (Color online) Experimental center-of-mass average velocity $\langle V_{c.m.} \rangle$ of fragments with atomic number $6 \leqslant Z \leqslant 28$ measured at various angles in the ^{78}Kr+^{40}Ca reaction at 5.5 MeV/nucleon.

B. Angular distributions

Valuable information on the production mechanism could be extracted from the angular distributions of the fragments. These distributions are obtained by integrating the kinetic-energy spectra. Some typical examples are given in Figs. 4 and 5 for various fragments.

The angular distributions of the fragments with atomic number close to the projectile one ($Z = 36$) are strongly peaked at forward angles as shown in Fig. 4. These products arise from direct two-body reactions or deep inelastic collisions in which nucleons are transferred into or emitted from the projectile. Indeed, in peripheral collisions the targetlike

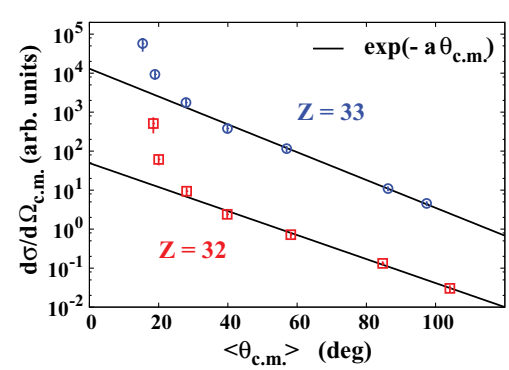

FIG. 4. (Color online) Angular distributions of fragments with atomic number $Z = 32$ and 33 produced in the ^{78}Kr+^{40}Ca reaction at 5.5 MeV/nucleon. The lines are exponential functions to guide the eye.

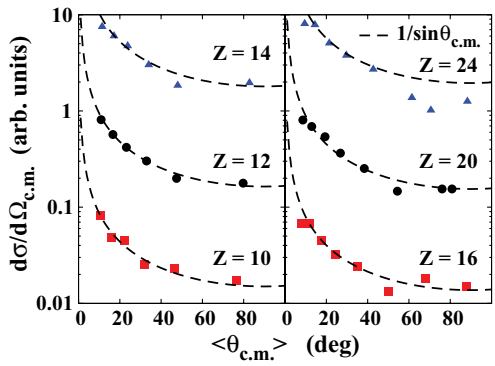

FIG. 5. (Color online) Angular distributions of fragments with charge $Z = 10, 12, 14, 16, 20, 24$ produced in the ^{78}Kr+^{40}Ca reaction at 5.5 MeV/nucleon. Dashed lines are $1/\sin\theta_{\text{c.m.}}$ functions that have been normalized to the experimental data at $\langle\theta_{\text{lab}}\rangle = 5.7^\circ$, corresponding to $\langle\theta_{\text{c.m.}}\rangle = 12^\circ$–$17^\circ$. Error bars are inside the symbols.

products are expected to be ejected in the backward hemisphere of the center of mass, while those coming from the projectile would be strongly focused in the forward hemisphere. Figure 4 illustrates such a behavior for $Z = 32$ and $Z = 33$ for which the angular distributions $d\sigma/d\Omega_{\text{c.m.}}$ exhibit a strong decrease. Moreover, one observes two components corresponding presumably to quasielastic reactions at the most forward angles and deep-inelastic collisions which dominate for $\theta_{\text{c.m.}} \gtrsim 20^\circ$. The continuous line in Fig. 4 represents an exponential function that follows the experimental data for $\theta_{\text{c.m.}} \gtrsim 20^\circ$.

In Fig. 5 we present the angular distributions $d\sigma/d\Omega_{\text{c.m.}}$ for fragments with atomic number $Z = 10, 12, 14, 16, 20, 24$ produced in the ^{78}Kr+^{40}Ca reaction. In spite of a measurement over a limited angular range in the laboratory frame, the reverse kinematics allows to define unambiguously the shape of the angular distributions in the center-of-mass frame. In contrast with the previously observed feature for fragments with $Z \sim 36$, the angular distributions follow a $1/\sin\theta_{\text{c.m.}}$ dependence (shown as dashed lines in Fig. 5). This signs a high degree of equilibration. Indeed, in heavy-ion reactions, CN that undergo fission have generally high angular momentum and the angular distributions of the fission fragments would show a $1/\sin\theta_{\text{c.m.}}$ shape. However, this kind of behavior is not a sufficient condition to ensure a CN formation. In fact, in quasifission (QF) process, the reactants retain some memory of the entrance channel which manifests in a strong anisotropy of the angular distribution [22]. Our apparatus does not allow an accurate measurement of the angular distributions of the fragments scattered at angles close to the beam direction. This prevents a dedicated investigation of the anisotropy. Thus at this stage of the analysis of the angular distributions presented in Fig. 5, one concludes that the predominant mode of the fragment production is the disintegration either of a long-lived system or CN.

C. Fragment-fragment coincidences

The correlations between the charge of the fragments are instructive since they permit us to check the binary nature of the mechanism. In the present work, an even-by-event analysis was performed in order to extract the two biggest fragments, i.e., those having the highest atomic numbers Z_1 and Z_2 (with $Z_1 \geqslant Z_2$) in each event. Figure 6 shows the Z_1 vs. Z_2 correlation measured in the ^{78}Kr+^{40}Ca reaction in the case of events satisfying the criterion $48 \leqslant Z_{\text{tot}} \leqslant 60$. The lower limit is applied to exclude the events in which one of the two fragments has not been detected. The upper limit take into account the uncertainty on the Z identification (see Sec. II). The highest yields are localized in two regions: $Z_1 \sim 50$ and $Z_2 \sim 2$ corresponding to the evaporation channel in one side; the region with Z_1, $Z_2 \sim 25$–30 representing the symmetric fragmentation mode in another side. The residues exclusively populated after light-particle emission could be well separated from those populated by IMF emission. This is important to underline since in case of a competition between CN and QF processes, one could unambiguously associate evaporation residues (ERs) with CN formation. The ridge of the counting rates seen in Fig. 6 is slightly shifted to an average value smaller by about two charge units than the total available charge ($Z = 56$), reflecting the light-particle emission from the fragments, and/or from the composite system before splitting. The linear correlation between Z_1 and Z_2 illustrates the binary nature of the mechanism. Here, the term binary means that the major part of the nucleons available in the reaction is distributed in the two biggest measured fragments.

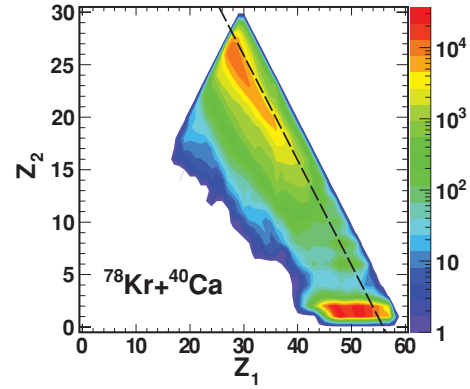

FIG. 6. (Color online) Experimental correlation between the two biggest fragments Z_1 and Z_2 with $Z_1 \geqslant Z_2$ and $48 \leqslant Z_{\text{tot}} \leqslant 60$.

As far as kinetic-energy spectra, angular distributions of the fragments and fragment-fragment coincidences are concerned, the same conclusions hold for ^{82}Kr+^{40}Ca reaction.

D. Cross sections

The absolute differential cross sections $d\sigma/d\Omega_{\text{c.m.}}$ were obtained from the normalization with respect to the elastic scattering. To select the appropriate angle for normalization purposes, both grazing angle and angular distribution of the elastic scattering were deduced from optical model calculations [35]. To do so, a set of optical parameters was extracted from the study of the Ar+Se reaction at 5 MeV/nucleon [36] that is similar to those studied in the present work. From the analysis, we deduced that the grazing angle is about $\theta_{\text{lab}} = 20^\circ$ (around $\theta_{\text{c.m.}} = 55^\circ$). Moreover, $\sigma/\sigma_{\text{Ruth}}(\theta_{\text{lab}}) = 1$ for $\theta_{\text{lab}} \leqslant 14^\circ$. Thus the Rutherford differential cross section of the

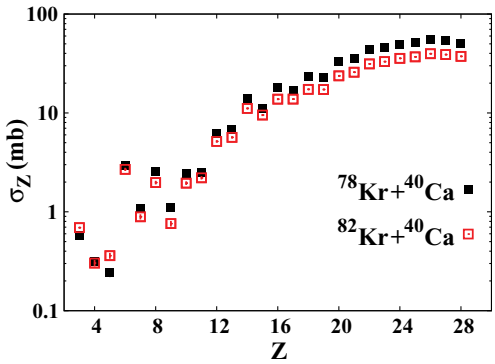

FIG. 7. (Color online) Experimental cross sections for fragments with atomic number $3 \leqslant Z \leqslant 28$ emitted in the ^{78}Kr+^{40}Ca (full squares) and ^{82}Kr+^{40}Ca (open squares) reactions at 5.5 MeV/nucleon.

elastic scattering was integrated over the range $7^\circ \leqslant \theta_{\rm lab} \leqslant 10^\circ$ to get the normalization factor. Then the absolute total cross sections of the fragments with atomic number $3 \leqslant Z \leqslant 28$ were obtained by angular integration assuming a $1/\sin\theta_{\rm c.m.}$ shape as indicated in Sec. III B. This procedure could not be suited to the nonmeasured part of the angular distribution close to the beam direction, but the weight of this angular domain is negligible. In the following, we concentrate on the decay behavior of a long-lived system, and consequently the cross sections of the quasielastic component are not discussed here due to the exponential shape of the angular distributions, akin to a fast process.

The inclusive cross sections σ_Z of fragments with atomic number $3 \leqslant Z \leqslant 28$ are shown in Fig. 7 for the ^{78}Kr+^{40}Ca (solid squares) and ^{82}Kr+^{40}Ca (open squares) reactions. Note that the Be cross sections are depleted due to the contribution of the nonidentified ^{8}Be fragment. The σ_Z distributions for both systems exhibit a maximum around $Z = 26$, a value close to half of the available charge. Such a feature indicates that these elements come either from the symmetric fission of CN or from a class of collisions in which a strong relaxation of the entrance channel mass asymmetry has been reached. Moreover, except for $3 \leqslant Z \leqslant 5$, σ_Z measured in the ^{82}Kr+^{40}Ca system is systematically lower and the yields around the symmetric splitting are about 25% smaller for the system having the highest neutron-to-proton ratio. Such a lowering of the cross section for the symmetric splitting as the neutron content of the emitter increases is also observed in ^{78,82,86}Kr+^{12}C reactions [3]. This N/Z dependence would be consistent with the expectations of the liquid-drop model in which the fission barrier of a neutron-poor CN is expected to be smaller than for the neutron-rich one, providing that these fissionlike fragments originate from CN decay.

A strong odd-even staggering (o-e-s) of the σ_Z for fragments with $Z \leqslant 10$ is visible, and this effect is still present for higher Z with a smaller amplitude. Fluctuations in fragment yields have already been observed in a wide range of reactions, from CN regime to spallation reactions [3,6,7,37,38]. It is worth noting that the staggering in the yields of light clusters shown in Fig. 7 is very similar to the one observed for systems in the same range of mass, excitation energy, and angular momentum [2,5]. This would indicate that the staggering is not preferentially driven by microscopic properties of the complementary partners since they differ for each studied reaction.

As shown in Fig. 7, the o-e-s for light fragments is roughly the same for both reactions and is about a factor 3. Such a result is at variance with ^{78,82,86}Kr+^{12}C data [3] for which the o-e-s decreases for neutron-rich CN. As far as the entrance channels are concerned, the main difference between those data and the present ones comes from the magnitude of the spin that could be transferred into the composite system. Thus, the o-e-s of the light-fragment yields could be influenced by the spin which would induce different compactness of the scission configurations and thus a sensitivity to structure properties in the deformation space.

As suggested by the shape of the Z distribution, the high partial waves in the entrance channel should have fed the fragment emission mechanism. However, the cross sections of the light clusters (Li, B) are astonishingly low. Indeed, in ^{93}Nb + ^{9}Be, ^{12}C reactions [4] in which low angular momentum were involved, the cross sections of the light clusters are of the same order of magnitude or even higher than in our measurements. A possible explanation would be that at high angular momentum a large part of the flux has been deviated from a CN formation. Such a possibility will be discussed in Sec. V.

The cross sections of the fissionlike products, $\sigma_{\rm fiss}^{\rm exp}$, were obtained by summing up the yields of the fragments in a range of atomic number $3 \leqslant Z \leqslant 26$. The upper limit corresponds to the atomic number of the fragments produced with the highest cross section and takes into account qualitatively the secondary decay of light charged particles (see Fig. 6). Thus, considering the range $3 \leqslant Z \leqslant 26$ we obtain $\sigma_{\rm fiss}^{\rm exp} = 447 \pm 46$ mb ($\sigma_{\rm fiss}^{\rm exp} = 332 \pm 35$ mb) for the ^{78}Kr+^{40}Ca (^{82}Kr+^{40}Ca) reactions, respectively. We note here that we have termed as fissionlike products those with an angular distribution akin to that of a long-lived system, and $\sigma_{\rm fiss}^{\rm exp}$ could contain both CN and QF contributions.

The ER component is identified thanks to a ΔE-E two-dimensional plot using the energy deposited in the IC and Si detectors. Absolute differential cross sections $d\sigma_{\rm ER}/d\Omega_{\rm lab}$ are deduced from the normalization with respect to the elastic scattering. Since $d\sigma_{\rm ER}/d\Omega_{\rm lab} \approx \exp[-k\sin^2\theta_{\rm lab}]$ [39], the experimental distribution is extrapolated toward the beam direction, and $\sigma_{\rm ER}^{\rm exp}$ could be extracted. Extensive simulations using statistical code PACE4 [40] were performed to check this procedure. We obtain $\sigma_{\rm ER}^{\rm exp} = 539 \pm 100$ mb ($\sigma_{\rm ER}^{\rm exp} = 492 \pm 90$ mb) for the ^{78}Kr+^{40}Ca (^{82}Kr+^{40}Ca) reactions, respectively. These cross sections together with $\sigma_{\rm fiss}^{\rm exp}$ are gathered in Table II.

The sum of the fissionlike and ER cross sections defines the experimental capture cross sections $\sigma_{\rm capt}^{\rm exp} = \sigma_{\rm ER}^{\rm exp} + \sigma_{\rm fiss}^{\rm exp}$ and we measured $\sigma_{\rm capt}^{\rm exp} = 986 \pm 110$ mb ($\sigma_{\rm capt}^{\rm exp} = 824 \pm 97$ mb) for the ^{78}Kr+^{40}Ca (^{82}Kr+^{40}Ca) reaction, respectively. By using the sharp cutoff approximation formula

$$\sigma_{\rm capt}^{\rm exp}(E_{\rm c.m.}) = \frac{\pi\hbar^2}{2\mu E_{\rm c.m.}} \sum_{J=0}^{J_{\rm max}} (2J+1) = \frac{\pi\hbar^2}{2\mu E_{\rm c.m.}} (J_{\rm max}+1)^2, \quad (1)$$

TABLE II. Measured and calculated evaporation residues and fissionlike cross sections. See Sec. V for details of the calculations performed with GEMINI and DNS codes.

(mb)	^{78}Kr+^{40}Ca	^{82}Kr+^{40}Ca
$\sigma_{\rm fiss}^{\rm exp}$	447 ± 46	332 ± 35
$\sigma_{\rm ER}^{\rm exp}$	539 ± 100	492 ± 90
$\sigma_{\rm fiss}^{\rm GEMINI}$	600	547
$\sigma_{\rm ER}^{\rm GEMINI}$	237	285
$\sigma_{\rm fiss}^{\rm DNS}$	349	208
$\sigma_{\rm ER}^{\rm DNS}$	601	638

we obtained $J_{\rm max}^{\rm exp} = 75 \pm 4$ (70 ± 4) for the ^{78}Kr+^{40}Ca (^{82}Kr+^{40}Ca) reaction, respectively.

From the ER cross sections we have calculated the reduced quantity $\Lambda_{\rm ER} = 2\mu E_{\rm c.m.}\sigma/(\pi\hbar^2)$, in which the dependence on the entrance channel is removed. In the literature we have extracted the same quantity for reactions similar to those studied here. The $\Lambda_{\rm ER}$ values for ^{78,82}Kr+^{40}Ca reactions are compatible with the data for the quasi-symmetric entrance channel such as, for example, ^{58}Ni+^{64}Ni [41] or ^{52}Cr+^{56}Fe [42] and the mass-asymmetric system such as the ^{32}S+^{76}Ge [43] reaction. However, the $\Lambda_{\rm ER}$ values for ^{78,82}Kr+^{40}Ca reactions are smaller than the one extracted for other mass-asymmetric systems such as ^{16}O+^{92}Mo [42] and ^{32}S+^{100}Mo [44]. This would indicate a different boundary between evaporation and fissionlike channels in the J space as a function of the mass asymmetry of the entrance channel, as, for example, when fusion and quasifission processes compete with each other.

The capture cross section in the ^{78}Kr+^{40}Ca reaction is higher than the one measured in the ^{82}Kr+^{40}Ca reaction. This behavior is at variance with observations in the vicinity of the Coulomb barrier for systems with similar masses ([45–47]). Considering these measurements at the highest bombarding energy (~10% above the Coulomb barrier), $\sigma_{\rm capt}^{\rm exp}$ of a neutron-rich system (^{36}S+^{96}Zr) exceeds by ~25% the capture cross-section of a neutron-poor system (^{36}S+^{90}Zr) and the same trend is observed for the ^{32}S+^{90,96}Zr reactions. However, in these cases the cross sections of fissionlike products were negligible while this decay mode accounts for almost 50% of $\sigma_{\rm capt}^{\rm exp}$ in the ^{78,82}Kr+^{40}Ca reactions at 5.5 MeV/nucleon. In the reactions studied here, the difference in $\sigma_{\rm capt}^{\rm exp}$ is mainly due to the fissionlike component, leading to a smaller capture cross section for the ^{82}Kr+^{40}Ca system. The confrontation with the predictions of theoretical models will bring more information to discuss this aspect.

IV. FRAGMENT-PARTICLE COINCIDENCE MEASUREMENTS

To better understand the fragment emission mechanism and to get more insights on the o-e-s of the light-fragment yields, we have performed an event-by-event analysis of the light charged particles (LCPs) in coincidence with fragments. In the first step, we calculated for each fragment the relative velocity between that fragment and each detected LCP of the event. Then we consider a new frame with one axis corresponding to the direction of the fragment velocity in the center-of-mass frame and the plane perpendicular to this axis. Finally, we projected the relative velocities previously calculated onto this new frame and deduced the component parallel ($V_\parallel$) and perpendicular ($V_\perp$) with respect to the direction of the fragment velocity in the center-of-mass frame. In doing so, for fragments of a given Z, having different emission angles in the center of mass, the procedure enables to construct a common reference frame for the LCPs in coincidence with these fragments. We have seen the binary nature of the fragment production with a small amount of particles emitted meanwhile. Thus, the kick induced by the emitted particles should be small and one could assume that fragments are flying back to back in the center of mass. The emission direction of one fragment then defines the recoil direction of its complementary partner. With such a method applied to an ensemble of reactions, the particles emitted by one fragment with a constant velocity value will draw one circle centered at the origin of the reference frame in a $V_\parallel$-$V_\perp$ plot.

Figure 8 presents typical examples of $V_\parallel$-$V_\perp$ diagrams for α-C (first row), α-Si (second row), and α-Fe (third row) coincidences measured in the ^{78}Kr+^{40}Ca reaction. The black circles represent the average velocities taken from systematics compiled by Parker *et al.* [48]. For α-C coincidences, the relative velocities draw a circular region (akin to a Coulomb ring) which is centered at the origin when they are projected into the frame (termed the Compl frame) of the complementary

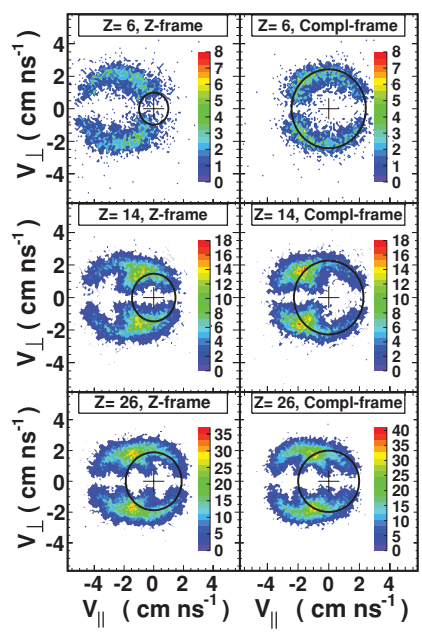

FIG. 8. (Color online) $V_\parallel$-$V_\perp$ diagrams of α particles detected in coincidence with C (first row), Si (second row), and Fe (third row) fragments produced in ^{78}Kr+^{40}Ca reaction at 5.5 MeV/nucleon (see text). The velocities are calculated in the reference frames of the light fragment (left panels) and of the complementary fragment (right panels).

partner of the C nuclei (top right panel), whereas no such circular region centered at the origin can be seen when the relative velocities are plotted in the frame (termed the Z frame) of the light partner (top left panel). For $Z = 14$ and 26, both fragments emit light particles as illustrated by the two circles centered at both reference frames. Thus, we observe the change of behavior of the light-particle emission from very asymmetric ($Z = 6$) to asymmetric ($Z = 14$) and almost symmetric ($Z = 26$) fragmentation. The same conclusions hold for fragment-proton coincidences. Thus, in ^{78}Kr+^{40}Ca reactions at 5.5 MeV/nucleon, the LCPs are emitted by both fragments in the case of symmetric fragmentation, whereas for a very asymmetric fragmentation, only the heavy fragment emits particles. The main lesson to be learned is that the light fragments are either produced cold or at excitation energies below the proton or α emission thresholds. Extensive simulations were performed in order to check that these results are not related to the geometrical acceptance since the present analysis has been performed with fragments and particles detected at $3^\circ \leqslant \theta_{\rm lab} \leqslant 70^\circ$. Such a limited angular range prevents to extract quantitative information on emission characteristics such as multiplicity of light-charged particles associated to each fragment pair. This kind of analysis will be presented in a forthcoming paper.

The broken dashed line in Fig. 9 shows the proton separation energy S_p calculated for the most abundant element given by the mass tables. A strong o-e-s is observed for S_p with roughly the same magnitude over the range $6 \leqslant Z \leqslant 28$. It is worth noting that the o-e-s of S_p and σ_Z are in phase each other. For light fragments both σ_Z and S_p are larger for even-Z. One can make an estimation of the excitation energy E_Z^* stored in the fragments. The total kinetic energy released in the binary fragmentation could be deduced from the kinetic energy of the light partner for which the mass number is calculated assuming that its N/Z ratio is the same as the composite system. By assuming a rigid rotation and a thermal equilibrium between both partners one can deduce E_Z^* from the energy balance. The results of such calculations are shown in Fig. 9 for an initial angular momentum of 40 (thin line) and 60 (thick line). E_Z^*

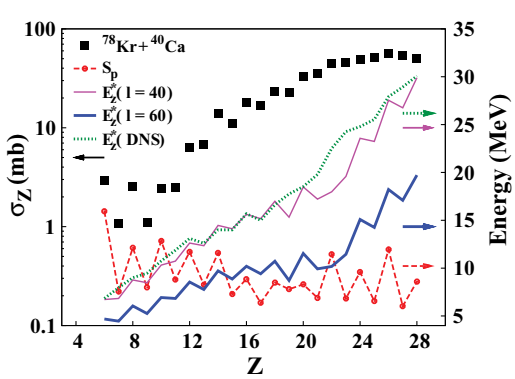

FIG. 9. (Color online) Experimental cross sections for fragments emitted in ^{78}Kr+^{40}Ca (solid squares) reactions at 5.5 MeV/nucleon. The broken dashed line represents the proton separation energy. Thin (thick) lines refer to the excitation energy stored in the fragment assuming an initial spin of 40 (60) respectively. Dotted line shows the DNS calculations.

increases almost constantly from about 8 MeV for $Z = 8$ to about 30 MeV for $Z = 28$. The staggering of E_Z^* is due to the fact that isotopic distribution for a given Z is not taken into account. The values of E_Z^* for $Z \leqslant 12$ are below 15 MeV, i.e., do not exceed the separation energy. One should note that the particle-fragment Coulomb barrier is not included, as it would have been done to estimate the emission energy thresholds. However, taking into account the Coulomb barrier would not change drastically the pattern since the Coulomb energy grows smoothly with the atomic number of the fragment.

The attenuation of the staggering of σ_Z for fragments having large Z would be related to a blurring due to light-particle emission as suggested by the coincidence data and by the estimation of E^* for symmetric fragmentation. The same conclusions hold when considering the separation energy of α particles. Thus, the σ_Z for light fragments reflect the persistence of structure effects in asymmetric fragmentation. This could be associated to a microscopic contribution to the potential energy surface that is a key ingredient in determining the fragment yields and/or to specific properties of the level density at energy below the particle emission thresholds. Such influences need further investigation.

V. COMPARISON WITH MODELS

In this section we compared data and the predictions of three theoretical approaches: two of them describe the decay modes of CN while the third one treats the dynamical evolution of the interacting partners and the physics governing the CN formation. Comparison of preliminary data and the dynamical cluster-decay model assuming preformed clusters [13] has been presented in Ref. [14].

A. Comparison with BUSCO

The Hauser-Feschbach approach is very successful in computing the light-particle emission from CN. In the BUSCO code [11], this formalism has been extended to the IMF emission in their ground states as well as excited states. In the version of the code we used in the present work, the emission of fragments up to $Z = 14$ has been incorporated. It should be noted that the fission channel is not taken into account. However, the model contains interesting features that justify the comparison to the present data, providing that the CN spin distribution is given by the sharp cutoff approximation with $J_{\rm max}$ kept as a free parameter.

The decay width of a channel α from a CN formed at a spin J is given by [10,11]

$$P_\alpha^J = \sum_{l_\alpha} \int T_{l\alpha}(\epsilon_\alpha)\rho(E_{\rm CN}^* - \epsilon_\alpha, J)\, d\epsilon_\alpha. \qquad (2)$$

In Eq. (2), $T_{l\alpha}$ are the optical-model transmission coefficients evaluated at the relative kinetic energy ϵ_α in the emitter frame and ρ is the Fermi-gas model level density of the daughter nuclei computed with the prescription of Ref. [49]. The transmission coefficients have been parameterized by a

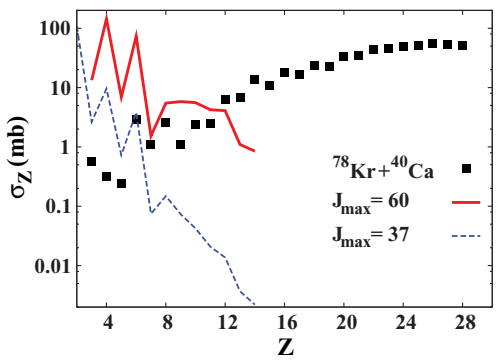

FIG. 10. (Color online) Experimental cross sections for fragments emitted in the ^{78}Kr+^{40}Ca reaction at 5.5 MeV/nucleon (squares), compared to BUSCO calculations assuming a J distribution given by the sharp cutoff approximation with $J_{\max} = 60$ (thick line) and $J_{\max} = 37$ (dashed line). Calculations have been performed with the level-density parameter $a = A/8.5$ MeV^{-1}.

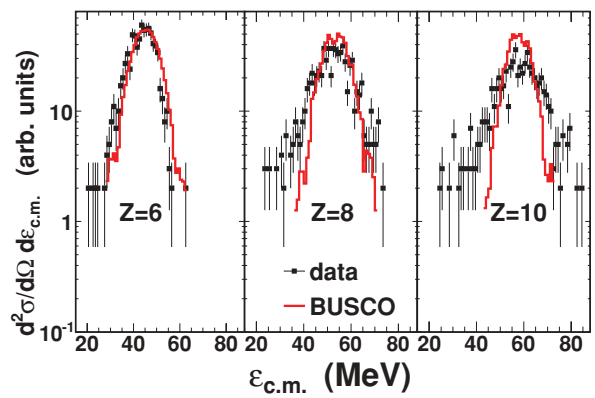

FIG. 11. (Color online) Kinetic energy spectra in the center-of-mass frame for $Z = 6, 8, 10$ emitted in the ^{78}Kr+^{40}Ca reaction. Histograms are data and dashed lines are the results from the BUSCO calculations using $J_{\max} = 60$ and a level-density parameter $a = A/8.5$ MeV^{-1}. Calculations were normalized to data assuming the same integral for each Z.

Fermi function

$$T_{l_\alpha}(\epsilon_\alpha) = (1 + \exp[-(B_{l_\alpha} - \epsilon_\alpha)/\Delta_\alpha B_{l_\alpha}])^{-1},$$

where

$$B_{l_\alpha} = B_0 + \hbar^2 l_\alpha(l_\alpha + 1)/2\mu R_\alpha^2.$$

The parameters B_0, R_α, and Δ_α are obtained from the best fits of optical-model transmission coefficients. The predictions of the model have been successfully compared to data in the medium-mass CN region [8,11,24].

The present calculations were performed using the level-density parameter $a = A/8.5$ MeV^{-1} and a sharp cutoff approximation with $J_{\max} = 60$ as a starting estimate. The results of the BUSCO calculations for the ^{78}Kr+^{40}Ca reaction are symbolized by a thick line in Fig. 10. The model fails to reproduce the features of the Z distribution, although an odd-even staggering as in the data is seen for $Z \leqslant 8$. For $Z \leqslant 14$ one observes a global decreasing of the calculated σ_Z at variance with data. More specifically, the cross section of C is overestimated by a factor 30, while σ_Z for $8 \leqslant Z \leqslant 12$ are overestimated within a factor of 2 to 6. A calculation assuming $J_{\max} = 37$ (dashed line in Fig. 10) in order to reproduce σ_Z for C largely misses the yields of the other species. Taking a J distribution with a diffuseness around $J_{\max}$ instead of a sharp cutoff approximation or making different choices of the level-density parameter do not improve the predictions of the model.

Since the interaction barriers play a crucial role in the competition between the decay channels, we compared the calculated kinetic-energy spectra of the fragments to the experimental data. In the BUSCO code, the kinetic-energy spectra result from the folding of the optical-model transmission coefficients and the level density. Thus the shape of the spectra is a good test of the calculation. The comparison of theoretical and measured spectra is presented in Fig. 11 for $Z = 6, 8, 10$. For each Z, the calculation was normalized to the integral of the kinetic energy distribution. The agreement is very good for the mean kinetic energy. However, the calculated width of the distribution is smaller. The same conclusion holds for other fragments. Improvement of the calculated kinetic-energy spectra could be obtained by a fine-tuning of the parameters, but the isotopic distribution is unknown and such a fitting procedure would not be under control. We thus conclude that the basic ingredients to estimate the kinematics seem to be reasonably implemented.

A possible explanation of the disagreement with the experiment would be the too-small number of excited states $n_{\rm ex}$ incorporated into the calculation. Indeed, for the ^{12}C nucleus, $n_{\rm ex} = 5$ are included up to 16.7 MeV; for ^{16}O, $n_{\rm ex} = 7$ up to 19.2 MeV and $n_{\rm ex} = 7$ up to 18 MeV for ^{28}Si. Such a reduced number of excited states may strongly affect the fragment cross sections, more specifically the yields of light clusters with respect to the heavy ones, and the production of odd- and even-Z and/or N nuclei. For example, there are 60 states below 8.32 MeV in ^{19}F, 103 states below 13.97 MeV in ^{20}Ne, 160 states below 8.19 MeV in ^{26}Al and 62 states below 11.59 MeV in ^{28}Si [50]. Considering a small number of excited states $n_{\rm ex}$, the code BUSCO would amplify the effect of the Q values and barriers which could explain the abrupt decrease of the cross sections of the light fragment. Addition of further excited states could be envisaged but the upper limit of the fragments to be considered in the calculation and the treatment of the fission channel are still important open questions yet to be resolved.

B. Comparison with GEMINI

In their work, N. Bohr and A. J. Wheeler [51] recognized that the fission probability of a nucleus is governed by the number of states above the fission barrier and the saddle-configuration plays the role of a transition state between the CN and the scission-configuration. Moretto [52] extended this concept to the asymmetric-fission mechanism. The GEMINI code [33] combines Hauser-Feschbach and transition-state formalisms to describe the disintegration of a hot CN by emission of products spanning the whole mass (charge) range from neutron to the fragment corresponding to the symmetric fission. The evaporation channels include n, p, d, t, ^{3}He, and α particles. The emission of fragments with $Z \geqslant 3$ is described

within the transition-state model using the saddle conditional energy for different mass (or charge) asymmetries deduced from the finite-range rotating liquid-drop model [16].

The decay width for the emission of a fragment (Z, A) from a CN at excitation energy $E^*_{\rm CN}$ and spin J is written as

$$\Gamma_{Z,A}(E^*_{\rm CN}, J) = \frac{1}{2\pi\rho_0}\int_0^{E^*_{\rm CN}-E_{\rm sad}(J)} \rho_{\rm sad}(U_{\rm sad}, J)d\epsilon,$$

where $U_{\rm sad} = E^*_{\rm CN} - E_{\rm sad}(J) - \epsilon$ and $\rho_{\rm sad}$ are the thermal energy and the level density calculated at the conditional saddle-point configuration, respectively. ϵ is the kinetic energy and $E_{\rm sad}(J)$ is the energy of the saddle-point configuration calculated in the finite-range liquid-drop model of Sierk. Nuclear level densities are given by the Fermi-gas formula for a fixed angular momentum J as follows

$$\rho_{\rm sad}(U_{\rm sad}, J) \propto \frac{(2J+1)}{U^2_{\rm sad}} \exp[2\sqrt{(aU_{\rm sad})}].$$

In the model, the angular momentum $J_{\rm lim}\hbar$ at which the fission barrier disappears is $69\hbar$ for the ^{118}Ba nucleus and $74\hbar$ for the ^{122}Ba nucleus. In the case of the ^{122}Ba nucleus, $J_{\rm lim}$ is higher than $J^{\rm exp}_{\rm max}$ deduced from data, while $J_{\rm lim} < J^{\rm exp}_{\rm max}$ for the ^{118}Ba nucleus. Consequently, the calculations have been performed assuming a sharp cutoff for the angular momentum distribution with $J_{\rm max} = J_{\rm lim} = 69$ for the ^{78}Kr+^{40}Ca reaction and $J_{\rm max} = J^{\rm exp}_{\rm max} = 70$ for the ^{82}Kr+^{40}Ca reaction. Results of the calculations are reported in Fig. 12(a) for the ^{78}Kr+^{40}Ca system and in Fig. 12(b) for the ^{82}Kr+^{40}Ca reaction. As a first attempt we adopt a level-density parameter $a = A/8$ MeV^{-1}. The thick line in Fig. 12(a) presents the predictions for the disintegration of ^{118}Ba CN assuming $J_{\rm max} = 69$. The shape of the Z distribution for $12 \leqslant Z \leqslant 28$ is reasonably reproduced, although the model systematically underestimates the fragment yields in the range $18 \leqslant Z \leqslant 26$ by roughly 20%. A better agreement could be obtained by scaling the fission

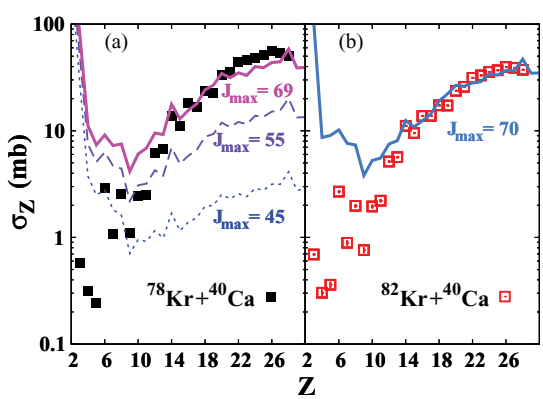

FIG. 12. (Color online) (a) Experimental cross sections for fragments emitted in the ^{78}Kr+^{40}Ca reaction (full squares) compared to the predictions of the GEMINI code assuming different maximum angular momenta: $J_{\rm max} = 69$ (thick line), $J_{\rm max} = 55$ (dashed line), and $J_{\rm max} = 45$ (dotted line). (b) Experimental cross sections for fragments emitted in the ^{82}Kr+^{40}Ca reaction (open squares) compared to the predictions of the GEMINI code assuming $J_{\rm max} = 70$ (thick line). Calculations were performed taking $a = A/8$ MeV^{-1} for the level-density parameter.

barriers but the examination of the whole Z distribution is more instructive. Indeed, the model overestimates by about a factor 10 the sum of the cross sections for $3 \leqslant Z \leqslant 11$. The difference comes mainly from the very high Li cross section, while C and O calculated yields are larger by about a factor 3. To give a flavor of the $J_{\rm max}$ dependence of the Z distribution, results for $J_{\rm max} = 55$ and $J_{\rm max} = 45$ are shown as dashed and dotted lines, respectively. C (Ne) yields are in satisfactory agreement for $J_{\rm max} = 45$ (55) but in both cases the whole shape is not correctly reproduced. This conclusion does not depend on the sharp cutoff approximation. Indeed, a smooth transition around $J_{\rm max}$ would degrade the global agreement since such a spin distribution tends to depopulate the region around the symmetry and, conversely, to increase the yield for Z around 16–20. In this way the net effect would be an increase of the width of the Z distribution and thus the agreement would become worse. Moreover, no major influence is observed by varying the level-density parameter from $A/7$ to $A/10$ MeV^{-1}. Regarding the staggering of the yields, one could observe a relatively good agreement above $Z = 10$, but the odd-even effect is not at all reproduced for the light fragments. The same conclusions could be written from the predictions of the disintegration of a ^{122}Ba CN [thick line in Fig. 12(b)]. In the range $12 \leqslant Z \leqslant 28$, the model reproduces the experimental data both in shape of the Z distribution and magnitude of the cross sections. As for the ^{78}Kr+^{40}Ca reaction, the model fails to reproduce the Z distribution for $3 \leqslant Z \leqslant 11$.

The pattern of the Z distributions for light fragments together with an overestimation of their yields might be due to a low barrier for mass-asymmetric fission. For medium-mass nuclei there is a quasidegeneracy of saddle and scission configurations, thus the total kinetic energy of the fragments is tightly related to the barrier. Considering the energy balance, a lower potential energy would correspond to higher excitation energy in the primary fragments. From the calculations, we deduced the primary Z distribution before secondary decays and the multiplicity of the particles emitted from each fragments. A careful analysis of the results indicates that, for $3 \leqslant Z \leqslant 11$, the initial smooth behavior of the Z distribution is modified by an emission of protons and α particles that finally induces the fluctuations of the calculated yields shown in Figs. 12(a) and 12(b). Thus, in the model, the fluctuations of the yields for light fragments are related to secondary emission of light particles, in contradiction with our data.

Last, the calculated ER cross sections $\sigma^{\rm GEMINI}_{\rm ER}$ for both systems (reported in Table II) are in the 250- to 300-mb range depending on the assumptions on the level-density parameter. These values are lower by about a factor 2 with respect to the experimental data. The low $\sigma^{\rm GEMINI}_{\rm ER}$ values could be related to the mass-asymmetric barrier that leads to enhance the light-fragment emission with respect to the evaporation of light particles.

Consequently, since the Z distribution mainly reflects the evolution of the barrier profile as a function of the mass asymmetry and angular momentum, the comparison with data would indicate a failure of the model to describe the boundary between asymmetric and symmetric fission at high angular momentum and that the landscape of the potential energy surface around symmetry would be steeper than the

one implemented in the GEMINI code. These conclusions hold if the decay products are unambiguously associated to CN disintegration. In this case, other potential-energy surfaces such as the one recently developed [53] might have a better behavior around symmetry as indicated in a recent investigation [54].

C. Comparison with the dinuclear system model

Both approaches presented in previous subsections treat the decay of an initial CN and disregard the collisional stage leading to its formation. However, a large body of data has reported on the competition between the fusion and the quasifission phenomena, the latter corresponding to the capture of interacting partners with a significant flow of matter and kinetic energy followed by a reseparation without being trapped in the CN configuration. For the interpretation of these two kinds of reactions, the new concept of the DNS has been developed and successfully compared to collisions involving massive nuclei [55]. This model has been recently applied [15] to the decay of medium-mass excited nuclei formed at relatively low angular momentum. Here we compared the predictions of the DNS model to our data which indicate a strong relaxation at relatively high angular momentum and moderate excitation energy. A detailed description of the model can be found in Refs. [15,55]; only the most salient features are outlined.

The DNS model describes the evolution of the interacting nuclei along two degrees of freedom; the relative distance R between the center of the nuclei; the charge and mass-asymmetry degrees of freedom, which are defined here by the charge Z and mass A of the light partner of the DNS. After the dissipation of kinetic energy and angular momentum of the relative motion, the DNS is trapped in the pocket of the interaction potential between partners. Then, a statistical equilibrium is reached in the mass-asymmetry coordinate so the formation probability $P_{Z,A}$ of each DNS or CN configuration depends on the potential energy $U(R_m, Z, A, J)$, calculated with respect to the potential energy of the rotational CN, where R_m is the location of the minimum in the interaction potential. After the capture stage, there are nucleon drift and nucleon diffusion between the nuclei which constitute the DNS. Then, the excited DNS can decay with a probability $P^R_{Z,A}$ in the R coordinate if the local excitation energy of the DNS is high enough to overcome the barrier in the nucleus-nucleus potential. Ultimately, the system evolves either toward a CN configuration that subsequently decays, or to a DNS configuration. The latter process, in which a two-body configuration is kept all along the trajectory, is the quasifission phenomenon.

The emission probability $W_{Z,A}(E^*_{\rm CN}, J)$ of a fragment (Z,A) is calculated as the product of the DNS formation probability and the DNS decay probability:

$$W_{Z,A}(E^*_{\rm CN}, J) = \frac{P_{Z,A} P^R_{Z,A}}{\sum_{Z',A'} P_{Z',A'} P^R_{Z',A'}},$$

where the indexes Z' and A' go over all possible channels from the neutron evaporation to the symmetric splitting.

The probability $P_{Z,A}$ is the equilibrium limit of the master equation (see Refs. [15,55] for details) given by

$$P_{Z,A}(E^*_{\rm CN}, J) = \frac{\exp[-U(R_m, Z, A, J)/T_{\rm CN}(J)]}{1 + \sum_{Z'=2,A'} \exp[-U(R_m, Z', A', J)/T_{\rm CN}(J)]}.$$

The quasifission barrier $B^{\rm qf}_R$, calculated as the difference between the bottom of the inner pocket and the top of the external barrier, prevents the decay of the DNS along the R degree of freedom with the weight $P^R_{Z,A}$ given as

$$P^R_{Z,A} \sim \exp[-B^{\rm qf}_R(Z, A, J)/T_{Z,A}(J)],$$

where $T_{CN}(J)$ and $T_{Z,A}(J)$ are the temperatures of the CN and the DNS, respectively. The Fermi-gas model is employed to compute the temperature, with a level-density parameter a taken as the high excitation limit of Ref. [56] that means $a = 0.114A + 0.162A^{2/3}$. With this prescription we obtained $a = 17.34$ MeV^{-1} for the ^{118}Ba nuclei, equivalent to $a = A/6.8$ MeV^{-1}, a value close to those we used in BUSCO and GEMINI calculations.

In the DNS model, all the trajectories leading to CN and QF processes represent the capture phenomenon. The pocket in the nucleus-nucleus potential disappears at some critical value $J = J_{\rm cr}$ and the DNS formation is no longer possible at $J > J_{\rm cr}$. The critical value $J_{\rm cr}$ determines the capture cross section. The dominant reaction mechanism (CN or QF) strongly depends on the angular momentum. For the reactions studied here, the driving potential at low angular momentum shows that the CN configuration is energetically more favorable than any DNS configuration. At higher angular momentum, the driving potential has a minimum at the symmetric DNS and the charge (mass)-drift pushes the system toward symmetric configuration. Consequently CN configuration becomes energetically less favorable and the high partial waves lead to QF. However, both mechanisms coexist in a wide range of angular momenta. For example, in the case of the ^{78}Kr+^{40}Ca reaction at 5.5 MeV/nucleon, the evaporation residue component accounts for about 10% of the partial cross section at $J = 65$.

There are two important facets of the model. First, no *a priori* assumption is made on the relaxation of the N/Z degree of freedom. Indeed the N/Z equilibration is reached when the DNS is trapped. Second, the connection between binary decay and evaporation channel is provided in a straightforward way by the mass-asymmetry coordinate. So, in the DNS model, the competition between the decay channels is treated in a common framework.

Figure 13(a) [Fig. 13(b)] compares DNS predictions and data for the ^{78}Kr+^{40}Ca (^{82}Kr+^{40}Ca) reaction, respectively. For both reactions, the largest value of the angular momentum $J_{\rm max}$ is taken as the critical value $J_{\rm cr}$ according to the model. For the ^{82}Kr+^{40}Ca system, $J_{\rm max} = 70$ is the value deduced from the measured total cross section. Predictions with $J_{\rm max} = 65$ for ^{78}Kr+^{40}Ca reaction are shown for the sake of comparison. Last, the ^{8}Be cross section has been removed from the results of the calculations to permit the comparison with data.

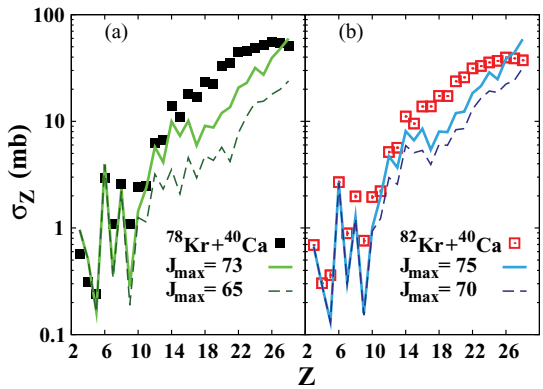

FIG. 13. (Color online) Comparison between measured and calculated cross sections. The calculated results with $J_{max} = 65$ ($J_{max} = 73$) for the ^{78}Kr+^{40}Ca reaction and $J_{max} = 70$ ($J_{max} = 75$) for the ^{82}Kr+^{40}Ca reaction are shown by dashed (solid) lines in panel (a) [(b)], respectively. Full (open) squares are data from the ^{78}Kr+^{40}Ca (^{82}Kr+^{40}Ca) reaction, respectively.

We observe a spectacular improvement with respect to the predictions of the BUSCO and GEMINI codes. Indeed, the DNS model satisfactorily reproduces the main features of the Z distributions. For both reactions, the shape of the Z distributions, the strong odd-even-staggering for $5 \leqslant Z \leqslant 10$, the small cross sections of light fragments as well as σ_Z around $Z = 28$ are well reproduced. However, for $16 \leqslant Z \leqslant 22$ the DNS model underestimates the fragment cross sections by about a factor 2 to 3. Since the whole capture cross section is considered, no improvement could be obtained within the present version of the model. Nevertheless, as reported in Table I, J_{cr} values of the DNS model are coherent with l_{pocket} calculated using the proximity potential. Moreover, the ER cross sections predicted by the DNS model σ_{ER}^{DNS} (see Table II) are compatible with the data, although the dependence of the ER cross section on the neutron-to-proton ratio does not follow the same trend as the one seen in the experiment. Thus, the depletion observed in the calculated yields for $16 \leqslant Z \leqslant 22$ might signal, in addition to the capture process, the presence of a class of deep-inelastic collisions associated to an incomplete relaxation of the entrance channel mass (charge) asymmetry and presumably localized in a J window just above J_{cr}. In this case the yields of the products near the entrance channel ($Z = 20$) can exceed the predictions of the DNS model.

The staggering of the yields decreases as the atomic number increases in agreement with the experimental findings. Since the pairing energy of the DNS light nucleus decreases with increasing mass number A, the odd-even effect becomes weaker for larger Z values. Moreover, the magnitude of the staggering is also influenced by the excitation energy stored in the primary fragments (see dotted line in Fig. 9). For nuclei with $Z \lesssim 10$ the calculated average excitation energy is below the particle emission threshold and these nuclei do not decay further except by γ emission which is not taken into account in the present version of the model. For heavy fragments, the average excitation energy and spin are high enough to open up the decay by light particles which strongly attenuates the odd-even structures of the Z distributions. Such results agree with our conclusions from the analysis of the fragment-particle coincidences. In agreement with data, σ_Z for fragments with $Z < 10$ are larger for the ^{78}Kr+^{40}Ca reaction. This can be explained by their smaller mass-asymmetric decay barriers for the reaction induced with ^{78}Kr projectile.

The calculated yields for $3 \leqslant Z \leqslant 10$ show a large odd-even-staggering of about a factor 10. Such o-e-s is much bigger than the experimental results and is mainly due to a strong underestimation of the odd-Z yields of B, N, and F while the C and O yields are well reproduced. The low predicted yields of the light fragments with odd-Z could be related to the prescription for the static deformation for odd nuclei that enter into the nucleus-nucleus potential.

Reasonable changes of static deformation would have minor effects on the yields. Another possibility would be the interplay between some microscopic properties (such as pairing interaction, for example) and deformation experienced by the dinuclear system en route to separation. Data would indicate an attenuation of these properties with deformation. Finally, the nuclear level densities below separation energy could play a role in the competition between channels since they could still retain some structure behaviors that are not included in the Fermi-gas approach [50].

Comparing the calculated cross sections for $J_{max} = 65$ and 73 ($J_{max} = 70$ and 75) for the ^{78}Kr+^{40}Ca (^{82}Kr+^{40}Ca) reactions [see Figs. 13(a) and 13(b), one can deduce that the contribution from high-partial waves to the yields for $Z \leqslant 10$ is negligible. The calculated partial production cross sections $\sigma_Z(E_{c.m.}, J)$ for some fragments from C to Ar are shown in Fig. 14 for the ^{78}Kr+^{40}Ca reaction at 5.5 MeV. We observed that most of the light fragments, as, for example, from C, O, or Ne, comes from angular momenta around $J\hbar \approx 40$–$60\ \hbar$. On the contrary, most of the heavy fragments, as, for example, from Cr, Fe, or Ni, are associated to partial waves around J_{max}. It is worth noting that $\sigma_Z(E_{c.m.}, J)$ develops two components for fragments with large Z showing a population through both CN and quasifission mechanisms. Examination of the results leads to the conclusion that QF is the dominant decay channel for heavy fragments while light fragments are predominantly populated by CN. Thus, the angular momentum strongly influences the competition between the binary decay channels and, correspondingly, the probability of light-fragment emission. One should also note that the careful identification of the origin of the binary decay products is a prerequisite before extracting information such as viscosity or fission barriers from fitting data. Thus, it would be very instructive to probe the competition between CN and QF components in the same mass region by studying small mass-asymmetric reactions where the flux going to CN is expected to dominate over a large range of incident partial waves. Experiments using a spin spectrometer with high capabilities [57] could be appropriate for such investigations.

The DNS model provides a good framework to describe both qualitatively and quantitatively fusion- evaporation cross sections as well as the main features of the yields of the light fragments such as C or O. The calculations confirm what we have deduced from the analysis of the fragment-light particle coincidences. The excitation energies and spins left in the heavy partners (Sn, Cd) after C or O emission are very high and

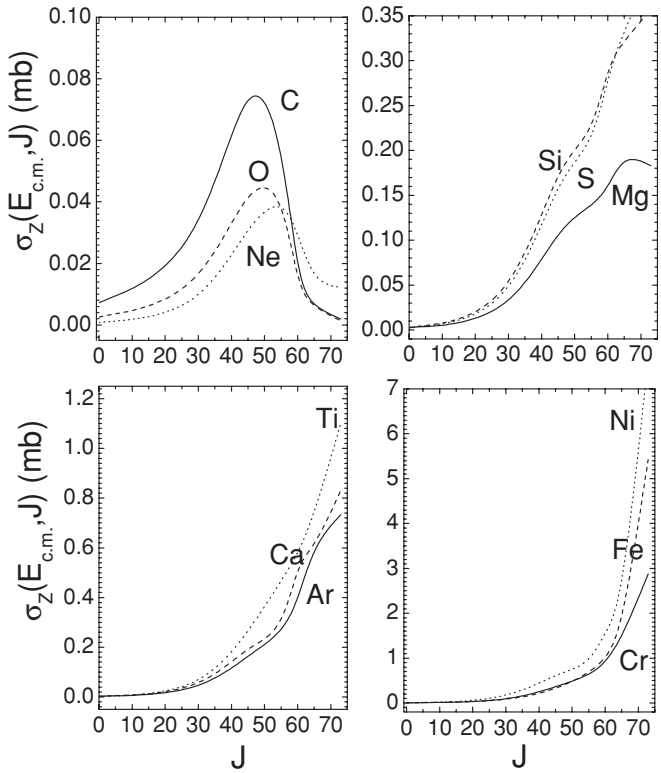

FIG. 14. Partial cross sections of the indicated fragments as a function of the angular momentum for the ^{78}Kr+^{40}Ca reaction at 5.5 MeV/nucleon.

since these heavy nuclei are neutron deficient, the secondary emission of light particles leads to the formation of residues of masses $A \sim 100$ with extremely small cross sections. We infer that better conditions could be obtained with reactions induced by a very neutron-deficient Kr beam at a bombarding energy close to the Coulomb barrier [58].

VI. SUMMARY AND CONCLUSIONS

We have presented the results of a study on decay modes of excited nuclei formed in ^{78,82}Kr+^{40}Ca reactions at 5.5 MeV/nucleon. The 4π INDRA array, which is very well suited to study the fate of violent collisions [59], has been exploited here in the low bombarding energy regime. The kinetic-energy spectra, the angular distributions, and the Z distribution for fragments with $3 \leqslant Z \leqslant 28$ show the characteristics of fissionlike phenomena. Analysis of the fragment-particle coincidences indicates that light partners in very asymmetric fission are produced either cold or at excitation energies below the particle emission thresholds. We observe a persistence of structure effects from elemental cross sections with a strong odd-even staggering for the lightest fragments. The magnitude of the staggering does not significantly depend on the neutron-to-proton ratio of the emitting system. The ER cross section of the ^{78}Kr+^{40}Ca reaction is slightly higher than the one measured in the ^{82}Kr+^{40}Ca reaction. The fissionlike component is larger by ~25% for the reaction having the lowest neutron-to-proton ratio. Last, the cross sections of the light clusters (Li, Be, B) are astonishingly low.

These experimental features were compared to the predictions of various theoretical approaches assuming either the formation of CN (BUSCO and GEMINI) or describing both the collisional stage preceding the CN formation and the competition with quasifission process (DNS model). The better global agreement is obtained within the DNS framework. For the ^{78,82}Kr+^{40}Ca reactions at 5.5 MeV/nucleon, the DNS model describes quantitatively the ER cross sections, the odd-even staggering of the light fragments and their low cross sections, as well as a large portion of σ_Z for $12 \leqslant Z \leqslant 28$. Finally, the features of the charge distribution for $3 \leqslant Z \leqslant 28$ are consistent with a strong competition between fusion-fission and quasifission processes. Examination of the results suggest that the quasifission mechanism is the dominant production mode for heavy fragments while light clusters are predominantly populated by decay of CN.

The confrontation with data confirms the crucial role of the mass- (charge) asymmetry degree of freedom on the disintegration of excited nuclei. Moreover, the potential energy surface that governs the evolution of the system must contain the contribution of microscopic properties of nuclei such as pairing interaction, shell effects, or static deformations. The interplay between the mass- (charge) asymmetry and N/Z degrees of freedom and their mutual influence on the competition between fusion evaporation reactions and binary decays is yet to be explored. The advent of powerful ISOL facilities will undoubtedly provide very well adapted opportunities to bring new insights on the respective role of the mass-asymmetry and N/Z degree of freedom during strongly dissipative collisions such as fusion and quasifission processes.

ACKNOWLEDGMENTS

We thank the staff of the GANIL facility for their support during the experiment and M. Loriggiola from LNL for providing us with Ca targets of excellent quality. We would like to acknowledge a number of very useful discussions with R. J. Charity, D. Lacroix, K. Mazurek, V. V. Sargsyan, and C. Schmitt. One of the authors (G. A.) gratefully acknowledges support by a research grant from the Conseil Régional de Basse Normandie, France, for carrying out this work. J.P.W. is indebted to people from Dubna-JINR, INFN-Sezione di Napoli and Università di Napoli "Federico II" for their warm hospitality. This work has been supported by the IN2P3-JINR, MTA-JINR, and Polish-JINR cooperation.

[1] L. G. Moretto and G. J. Wozniak, Prog. Part. Nucl. Phys. **21**, 401 (1988).
[2] L. G. Sobotka *et al.*, Phys. Rev. C **36**, 2713 (1987).
[3] K. X. Jing, L. G. Moretto, A. C. Veeck, N. Colonna, I. Lhenry, K. Tso, K. Hanold, W. Skulski, Q. Sui, and G. J. Wozniak, Nucl. Phys. A **645**, 203 (1999).

[4] R. J. Charity *et al.*, Nucl. Phys. A **483**, 371 (1988).
[5] J. Boger, J. M. Alexander, A. Elmaani, S. Kox, R. A. Lacey, A. Narayanan, D. J. Moses, M. A. McMahan, P. A. DeYoung, and C. J. Gelderloos, Phys. Rev. C **49**, 1597 (1994).
[6] T. S. Fan, K. X. Jing, L. Phair, K. Tso, M. McMahan, K. Hanold, G. J. Wozniak, and L. G. Moretto, Nucl. Phys. A **679**, 121 (2000).
[7] V. Ricciardi, A. V. Ignatyuk, K. Kelic, P. Napolitani, F. Rejmund, K.-H. Schmidt, and O. Yordanov, Nucl. Phys. A **733**, 299 (2004).
[8] J. Brzychczyk, D. S. Bracken, K. Kwiatkowski, K. B. Morley, E. Renshaw, and V. E. Viola, Phys. Rev. C **47**, 1553 (1993).
[9] H. Hauser and H. Feshbach, Phys. Rev. **87**, 366 (1952).
[10] R. G. Stokstad, in *Treatise on Heavy Ion Science*, edited by D. A. Bromley, Vol. III. (Plenum, New York, 1984).
[11] J. Gomez del Campo, R. L. Auble, J. R. Beene, M. L. Halbert, H. J. Kim, A. D'Onofrio, and J. L. Charvet, Phys. Rev. C **43**, 2689 (1991).
[12] F. Auger, B. Berthier, A. Cunsolo, A. Foti, W. Mittig, J. M. Pascaud, E. Plagnol, J. Québert, and J. P. Wieleczko, Phys. Rev. C **35**, 190 (1987).
[13] R. K. Gupta, M. Balasubramaniam, C. Mazzocchi, M. La Commara, and W. Scheid, Phys. Rev. C **65**, 024601 (2002).
[14] R. Kumar and R. K. Gupta, Phys. Rev. C **79**, 034602 (2009).
[15] Sh. A. Kalandarov, G. G. Adamian, N. V. Antonenko, and W. Scheid, Phys. Rev. C **82**, 044603 (2010).
[16] A. J. Sierk, Phys. Rev. Lett. **55**, 582 (1985).
[17] L. Corradi, *Proceedings of the Conference on New Aspects of Heavy Ion Collisions Near the Coulomb Barrier, Chicago, 2008*, AIP Conf. Proc. **1098**, 334 (2009).
[18] R. Bock, Nucl. Phys. A **388**, 334 (1982).
[19] B. B. Back, Phys. Rev. C **31**, 2104 (1985).
[20] J. Toke, R. Bock, G. X. Dai, A. Gobbi, S. Gralla, K. D. Hildenbrand, J. Kuzminski, W. F. J. Muller, A. Olmi, and H. Stelzer, Nucl. Phys. A **440**, 327 (1985).
[21] D. J. Hinde, M. Dasgupta, and A. Mukherjee, Phys. Rev. Lett. **89**, 282701 (2002).
[22] D. J. Hinde, A. C. Berriman, M. Dasgupta, J. R. Leigh, J. C. Mein, C. R. Morton, and J. O. Newton, Phys. Rev. C **60**, 054602 (1999).
[23] E. Prasad *et al.*, Phys. Rev. C **81**, 054608 (2010).
[24] J. Gomez del Campo *et al.*, Phys. Rev. C **57**, R457 (1998).
[25] M. La Commara *et al.*, Nucl. Phys. A **669**, 43 (2000).
[26] J. Pouthas *et al.*, Nucl. Instrum. Methods A **357**, 418 (1995).
[27] E. Bonnet *et al.*, Int. J. Mod. Phys. E **17**, 2359 (2008); J. P. Wieleczko *et al.*, *Proceedings of the Conference on New Aspects of Heavy Ion Collisions Near the Coulomb Barrier, Chicago, 2008*, AIP Conf. Proc. **1098**, 64 (2009); J. P. Wieleczko *et al.*, *Proc. Int. Conference on Nuclear Structure and Related Topics* (JINR, Dubna, 2009), p. 236; G. Ademard *et al.*, EPJ Web of Conferences **2**, 1402 (2010).
[28] G. Audi, A. M. Wapstra, and C. Thibault, Nucl. Phys. A **729**, 337 (2003).
[29] W. Reisdorf, J. Phys. G: Nucl. Part. Phys. **20**, 1297 (1994).
[30] I. Dutt and R. K. Puri, Phys. Rev. C **81**, 064609 (2010).
[31] KALIVEDA package [http://indra.in2p3.fr/KaliVedaDoc].
[32] J. D. Frankland *et al.*, Nucl. Phys. A **689**, 905 (2001).
[33] R. J. Charity *et al.*, Nucl. Phys. A **476**, 516 (1988).
[34] C. Beck and A. Szanto de Toledo, Phys. Rev. C **53**, 1989 (1996).
[35] The FRESCO code [www.fresco.org.uk].
[36] J. Galin, B. Gatty, D. Guerreau, C. Rousset, U. C. Schlotthauser-Voos, and X. Tarrago, Phys. Rev. C **9**, 1113 (1974).
[37] S. Steinhaüser *et al.*, Nucl. Phys. A **634**, 89 (1998).
[38] Sl. Cavallaro *et al.*, Phys. Rev. C **57**, 731 (1998).
[39] J. Gomez del Campo, R. G. Stokstad, J. A. Biggerstaff, R. A. Dayras, A. H. Snell, and P. H. Stelson, Phys. Rev. C **19**, 2170 (1979).
[40] O. B. Tarasov [www.nscl.msu.edu/tarasov/lise.html].
[41] K. E. Rehm, M. Paul, J. Gehring, B. Glagola, D. Henderson, W. Kutschera, and A. H. Wuosmaa, Nucl. Instrum. Methods A **344**, 614 (1994).
[42] S. Agarwal, J. Galin, B. Gatty, D. Guerreau, M. Lefort, X. Tarrago, R. Babinet, and J. Girard, Z. Phys. A **296**, 287 (1980).
[43] G. Guillaume, J. P. Coffin, F. Rami, P. Engelstein, B. Heusch, P. Wagner, P. Fintz, J. Barrette, and H. E. Wegner, Phys. Rev. C **26**, 2458 (1982)
[44] A. Brondi *et al.*, Annual Report LNL 2006 [www.lnl.infn.it/~annrep].
[45] A. M. Stefanini, L. Corradi, A. M. Vinodkumar, Y. Feng, F. Scarlassara, G. Montagnoli, S. Beghini, and M. Bisogno, Phys. Rev. C **62**, 014601 (2000).
[46] A. M. Stefanini *et al.*, Phys. Rev. C **73**, 034606 (2006).
[47] H. Q. Zhang *et al.* , Phys. Rev. C **82**, 054609 (2010).
[48] W. J. Parker *et al.*, Phys. Rev. C **44**, 774 (1991).
[49] A. Gilbert and A. G. W. Cameron, Can. J. Phys. **43**, 1446 (1965).
[50] T. von Egidy and D. Bucurescu, Phys. Rev. C **72**, 044311 (2005).
[51] N. Bohr and J. A. Wheeler, Phys. Rev. **56**, 426 (1939).
[52] L. G. Moretto, Nucl. Phys. A **247**, 221 (1975).
[53] K. Pomorski and J. Dudek, Phys. Rev. C **67**, 044316 (2003).
[54] K. Mazurek, C. Schmitt, J. P. Wieleczko, P. N. Nadtochy, and G. Ademard (submitted to Phys. Rev. C).
[55] V. V. Volkov, Izv. Akad. Nauk SSSR ser. fiz. **50**, 1879 (1986); G. G. Adamian, N. V. Antonenko, and W. Scheid, Nucl. Phys. A **618**, 176 (1997); G. G. Adamian, N. V. Antonenko, W. Scheid, and V. V. Volkov, *ibid.* **627**, 361 (1997); **633**, 409 (1998); A. S. Zubov, G. G. Adamian, N. V. Antonenko, S. P. Ivanova, and W. Scheid, Phys. Rev. C **68**, 014616 (2003); G. G. Adamian, A. K. Nasirov, N. V. Antonenko, and R. V. Jolos, Phys. Part. Nucl. **25**, 583 (1994); G. G. Adamian, N. V. Antonenko, R. V. Jolos, and A. K. Nasirov, Nucl. Phys. A **551**, 321 (1993).
[56] A. V. Ignatyuk, *Statistical Properties of Excited Atomic Nuclei* (Energoizdat, Moscow, 1983).
[57] See, for example [http://paris.ifj.edu.pl/].
[58] Sh. A. Kalandarov (private communication)
[59] B. Borderie and M. F. Rivet, Prog. Part. Nucl. Phys. **61**, 551 (2008).